A de novo metalloenzyme for cerium photoredox catalysis

Andreas Sebastian Klein[1,#], Florian Leiß-Maier[1,#], Rahel Mühlhofer[1], Benedikt Boesen[1], Ghulam Mustafa[1], Hannah Kugler[1], Cathleen Zeymer[1,2,*]

[1] Center for Functional Protein Assemblies & Department of Bioscience, TUM School of Natural Sciences, Technical University of Munich (TUM), Garching, Germany

[2] TUM Catalysis Research Center, Technical University of Munich (TUM), Garching, Germany

* E-mail: cathleen.zeymer@tum.de

[#] These authors contributed equally.

Abstract

Cerium photoredox catalysis has emerged as a powerful strategy to activate molecules under mild conditions. Radical intermediates are formed using visible light and simple complexes of the earth-abundant lanthanide. However, it remains a major challenge to achieve stereocontrol in these reactions. Here, we report an artificial photoenzyme enabling this chemistry inside a protein. We utilize a de novo designed protein scaffold that tightly binds lanthanide ions in its central cavity. Upon visible-light irradiation, the cerium-dependent enzyme catalyzes the radical C–C bond cleavage of 1,2-diols in aqueous solution. Protein engineering led to variants with improved photostability and initial stereoselectivity. The photoenzyme cleaves a range of aromatic and aliphatic substrates, including lignin surrogates. Surface display of the protein scaffold on *E. coli* facilitates whole-cell photobiocatalysis. Furthermore, we show that also natural lanthanide-binding proteins are suitable for this approach. Our study thus demonstrates a new-to-nature enzymatic photoredox activity with broad catalytic potential.

Introduction

Enzymes are highly efficient, selective, and sustainable catalysts. Their use in chemical and pharmaceutical industry increased substantially in recent years.[1] However, it remains challenging to develop enzymes that catalyze chemical reactions beyond nature's synthetic repertoire. To broaden the scope of biocatalysis, artificial metalloenzymes and photoenzymes have been generated by combining the catalytic strengths of transition metal cofactors and photosensitizers, respectively, with the selectivity of the chiral protein environment.[2,3] As these catalysts are genetically encodable, protein engineering can be applied to optimize efficiency and selectivity. To that end, rational enzyme design is often combined with subsequent directed evolution, which mimics natural selection in the laboratory.[4,5] Recent highlights include hetero-Diels-Alder reactions or [2+2] photocycloadditions catalyzed efficiently and with tight stereocontrol in a designed metalloenzyme or photoenzyme, respectively.[6-8]

Transition metal-dependent photoredox catalysis is a versatile strategy for the direct activation and functionalization of organic molecules using visible light.[9] Only recently, however, the field has started to exploit the photocatalytic potential of lanthanides.[10,11] These elements from the f-block of the periodic table mainly exist as trivalent cations that form structurally diverse complexes with high coordination numbers (CN = 8 to 12). Cerium has slightly different chemical and photophysical properties compared to the other elements of the 4f series. It is stable in two oxidation states (+III/+IV) and undergoes electronic transitions tunable by the chemical environment, which makes it attractive for photoredox catalysis. Compared to iridium or ruthenium used in classic photoredox catalysts, cerium is >10,000-fold more abundant in the earth's crust (ca. 65 ppm, similar to copper)[12] and may therefore be an ecologically and economically meaningful alternative. The emerging field of lanthanide photocatalysis is thus dominated by cerium photoredox chemistry, which offers two distinct mechanisms to generate reactive radical intermediates: (i) photoinduced ligand-to-metal charge transfer (LMCT) in Ce(IV) complexes and (ii) single electron transfer (SET) from Ce(III) in its excited state.

Recent studies have demonstrated the photocatalytic power and versatility of cerium complexes. For instance, the hexachlorocerate(III) anion $[Ce^{III}Cl_6]^{3-}$ is one of the most potent photoreductants with an excited state reduction potential $E_{1/2}^* = -3.05$ V vs. SCE.[13] It enables the reductive dehalogenation of chloroarenes and catalyzes Miyaura-type borylations of aryl halides under mild conditions.[14] Furthermore, the

alkylation, arylation, and amination of unactivated alkanes was achieved using cerium photoredox catalysis.[15,16] Mechanistic studies proposed either chlorine radicals or alkoxy radicals to be the catalytically relevant species.[17,18] While such reactive radicals can be generated under very mild conditions, it remains an unsolved problem to control their fate in subsequent reaction steps to enable stereocontrol in cerium photoredox catalysis. We hypothesized that this challenge can be tackled by performing this chemistry inside an enzyme.

Computationally designed proteins are particularly well suited for artificial metalloenzyme engineering, as their structure and geometry can be precisely tailored to enable selective metal binding.[19,20] These scaffolds are often also highly robust and, at the same time, catalytically naïve and evolutionarily unbiased. We recently explored de novo $(\beta\alpha)_8$ barrels,[21] so-called TIM barrels, as a potential platform for lanthanide binding.[22] To design an optimal coordination environment, we drew inspiration from nature, where lanthanide-dependent proteins and enzymes from certain methylotrophic bacteria possess binding sites with a spherical arrangement of several coordinating carboxy groups.[23-25] We thus installed four glutamate residues in the center of a symmetric de novo TIM barrel, which is formed from two $(\beta\alpha)_4$ half-barrels tethered to a lid domain (TIM-ferredoxin dimer = TFD).[22] Its specific lanthanide coordination was demonstrated by tryptophan-enhanced terbium(III) luminescence and X-ray crystallography (**Figure 1a**).The dimeric de novo protein binds lanthanides with femtomolar affinity[26] and remains folded at up to 95 °C and in up to 40% acetonitrile. It possesses an internal cavity above the metal binding site that could serve as a reaction chamber. With these properties, it provided an ideal starting point for us to engineer the first lanthanide-dependent photoenzyme.

Results

A cerium-bound de novo protein catalyzes the radical C-C bond cleavage of 1,2-diols with visible light

To demonstrate the feasibility of cerium photoredox catalysis in our de novo protein, we chose the radical C–C bond cleavage of 1,2-diols as a model reaction. This transformation was recently reported to occur photocatalytically in the presence of $CeCl_3$ in organic solvent with visible light.[27] It is proposed to proceed via β-scission of alkoxy radicals formed upon photoinduced LMCT, while the regeneration of Ce(IV) requires SET to atmospheric oxygen (**Figure 1b**). The cleavage of hydrobenzoin (**1**) in aqueous buffer with $CeCl_3$ yielded only trace amounts of the product benzaldehyde (**2**). In contrast, our lanthanide-binding TFD protein, now dubbed "*PhotoLanZyme* 1.0" (**PLZ1.0**), was indeed capable of catalyzing this reaction (**Figure 1c**). We found that wavelengths of 420 nm and below gave the highest yields, which is in agreement with the absorption of Ce(IV) in aqueous buffer (**Figure S2**). Furthermore, light on/off kinetics showed that the reaction only proceeds in the light (**Figure S6**). Importantly, no significant turnover was observed for all negative controls: in the absence of light, $CeCl_3$ or oxygen, and when using a knock-out variant in which all coordinating glutamates were replaced by glutamines (**PLZ1.0_KO**). To support the proposed radical mechanism, we performed the reaction in the presence of (2,2,6,6-tetramethyl-piperidin-1-yl)oxyl (TEMPO) as a radical scavenger, leading to significantly reduced product formation (**Figure 1c**). These results demonstrate that catalysis in aqueous solution requires cerium, light, oxygen, and specific metal coordination inside the protein.

Protein engineering improves photostability and metal binding kinetics

Next, we set out to improve the photoenzyme by protein engineering. To be able to generate asymmetric enzyme variants, we engineered a single-chain version of the protein scaffold, named **PLZ1.1**. To that end, the C-terminus of one subunit of the homodimeric **PLZ1.0** was covalently linked via a single glycine with the N-terminus of the other one.

When analyzing the enzymes' performance, we identified three main problems: (i) the protein suffered from severe photodamage, (ii) cerium binding to the active site was very slow and (iii) a substantial fraction of metal interacted unspecifically with the protein surface. We hypothesized that photodamage may be initiated by the

photooxidation of tryptophans, which is a well-known photochemical process (**Figure S7**).[28-30] Two such residues were originally installed directly next to the lanthanide binding site to facilitate tryptophan-enhanced terbium luminescence as a readout for metal binding. We sequentially mutated these positions, generating **PLZ1.2** and **PLZ1.3**. Furthermore, these variants carry two additional mutations rationally introduced to increase the asymmetry of the active site with the intention to enable stereocontrol. We characterized the photodamage of all cerium-bound PLZ variants after overnight irradiation using gel electrophoresis (SDS-PAGE), analytical size-exclusion chromatography (SEC), and mass spectrometry (ESI-MS). Here, **PLZ1.0** showed the most severe effects, including multiple oxidations with Δm = 16 Da, truncation after a tryptophan residue close to the C-terminus, as well as covalent crosslinking of the truncated monomers (**Figure 2a-c** and **Figure S8**). In contrast, variants without active-site tryptophans were significantly more photostable. This was further quantified by determining reaction yields after pre-irradiating the cerium-bound proteins for 24 hours prior to substrate addition (**Figure 2d**).

Lanthanide binding to the active site can be monitored spectroscopically with $TbCl_3$ in all variants with an active-site tryptophan (**Figure S9**). Here, we observed very slow binding kinetics at room temperature and essentially no signal increase at 4 °C (**Figure 2e** and **Figure S10**)**.** From 40 °C, however, metal binding was significantly more efficient. For all further reactions, we thus incubated the proteins with $CeCl_3$ at 40 °C for 2.5 hours prior to substrate addition. Furthermore, we observed unspecific cerium binding on the protein surface, which led to background activity in the KO variants. This effect could be suppressed by buffer-exchange over a desalting column to remove the weakly binding metal fraction prior to photocatalysis. Still, this procedure is not feasible when screening several enzyme variants in parallel using microtiter plates. We thus decided to re-engineer the protein surface. To that end, we identified clusters of negatively charged residues, which were predicted to bind metal according to the software tool *BioMetAll*,[31] and then introduced eight mutations (6x D to N and 2x E to Q) to minimize lanthanide binding to the protein surface (**Figure S11**). This led to a high terbium luminescence signal directly after mixing, indicating that less metal is bound unspecifically (**Figure 2e**).

The optimized variant **PLZ1.4** combines increased photostability with improved metal binding properties and was thus characterized in more detail. Overnight photoreactions with 5 mol-% enzyme gave up to 80% yield. The enzyme's total turnover number was

determined to be TTN = 78 ± 5 (**Figures S12**). We also measured Michaelis-Menten kinetics for diol substrate **1** and determined k_{cat} = 5.3 ± 0.2 h^{-1} and K_M = 2.9 ± 0.4 mM (**Figure 2f**).

The chiral protein environment enables initial stereocontrol

With the optimized photoenzyme **PLZ1.4** in hand, we started exploring its substrate scope (**Table 1** and **Figures S13-S31**). Aromatic substrates and products could be detected directly using their UV absorption, while the aldehydes produced from aliphatic substrates were derivatized with 2-amino-benzamidoxime (ABAO) prior to HPLC analysis (**Figures S3/S4**).[32] For hydrobenzoin (**1**) and 1-phenyl-1,2-ethanediol (**3**), all stereoisomers were separately available, but other substrates were handled as mixtures of stereoisomers. We screened several substituted aromatic diols (**4, 6, 8**) and found similar yields as observed for hydrobenzoin (**1**). Tertiary diol **10** was less well accepted. Single aromatic alcohols (**12, 14**) and aliphatic diols (**15, 17**) also gave lower yields. Interestingly, substrates **12** and **19** yielded a product mixture consisting of benzaldehyde (**2**) and benzyl alcohol (**13**), while the cleavage of the aromatic amino alcohol **21** gave two molecules of **2** (see **Figure S34** for mechanistic proposals).

We were most interested in identifying initial stereoselectivity enabled by the chiral protein environment and thus compared the turnover rates of **(*R,R*)-1**, **(*S,S*)-1** and ***meso*-1** premixed in a single reaction vial. While a pronounced diastereoselectivity was observed, no enantioselectivity could be detected (**Figure S32**). However, when separating the reaction mixture after the photocatalytic cleavage of 1,4-diphenylbutane-2,3-diol (**19**) on a chiral column, we reproducibly saw an enantiomeric excess (*ee*) for the unreacted substrate (**Figure 3a**). The stereoisomers in the chiral HPLC traces were assigned using authentic standards (**Figure S33**). Notably, also the initial single-chain variant **PLZ1.1** showed a low selectivity, albeit with preference for the opposite enantiomer. These results strongly indicate that our photocatalytic reaction indeed happens inside the protein and that its stereochemical outcome is influenced by the binding pocket.

We obtained an AlphaFold2[33,34] model of **PLZ1.4** (**Figure S46**), which closely resembles the overall structure of **PLZ1.0**,[22] and performed substrate docking for substrate **19** (**Figure 3b** and **Figure S48**). The central cavity of the enzyme is large and the two domains are tethered by flexible linkers, which allows for several substrate conformations of all three stereoisomers to bind with similar binding energy and thus

explains the low enantioselectivity (**Video S1**). However, based on these results, rational engineering and directed evolution can be performed synergistically in the future to improve activity and selectivity.

The photoenzyme cleaves lignin surrogates and can be used for whole-cell photobiocatalysis

Aromatic diol motifs are found in lignin, a complex organic polymer that together with cellulose is responsible for the structural integrity and rigidness of plant cell walls, especially in wood (**Figure 4a**). It is one of the most abundant renewable resources for aromatic compounds and its chemical or enzymatic degradation is a promising way towards valorization.[35-37] We thus asked whether our photoenzyme would also accept lignin surrogates (**22, 23, 24**).[38,39] The three substrates we tested all yielded benzaldehyde (**2**) as the major degradation product after enzymatic cerium photoredox catalysis using purified **PLZ1.4** (**Table 1**). For substrate **24**, we also measured enzyme kinetics with k_{cat} = 1.5 ± 0.2 h^{-1} and K_M = 5.5 ± 1.0 mM (**Figure S37**).

Interestingly, the HPLC trace for 1,3-diol **22** showed 1,2-diol **3** as a reaction intermediate, which is then cleaved one more time to give a second equivalent of benzaldehyde (**2**). To investigate this mechanism further, we performed trapping experiments with TEMPO (**Figure S35**). The results clearly confirmed the presence of two benzylic radicals (identified as TEMPO adducts by LC-MS), which are then hydroxylated to form intermediate **3**. To test whether the respective oxygen atom originates from water or molecular oxygen, we set up photoenzymatic reactions in $H_2{}^{18}O$ (**Figure S36**). Here, we observed quantitative ^{18}O-isotope labeling of the product benzaldehyde (**2**). However, this can also be explained plausibly by a simple exchange with water after the reaction. We thus tested also the cleavage of substrate **12** in $H_2{}^{18}O$, where benzyl alcohol is formed that cannot undergo this exchange. Here, we found exclusively benzyl alcohol with ^{16}O, not ^{18}O, indicating that the benzylic radicals react with molecular oxygen, but not water.

The photoenzymatic degradation of lignin would be most economical if whole-cell biocatalysis was established. This would require artificial metalloenzyme formation in the cellular environment. We thus explored a cell surface display approach. We generated a fusion construct in which **PLZ1.1** is attached to a Lpp-OmpA sequence (**Figure 4b**), described previously for surface display of an artificial metalloenzyme on *E. coli* cells.[40] The successful display was verified by detecting a C-terminal HA tag in

both Western blot analysis after cell fractionation and fluorescence microscopy (**Figure 4c/d and Figures S38/S39**). We found that lignin surrogate **24** was efficiently degraded to benzaldehyde using whole cells treated with $CeCl_3$ in the presence of visible light. Here, the surface display construct was compared to several controls, including cells expressing the enzyme cytoplasmically, an Lpp-OmpA construct without the enzyme, and uninduced *E. coli* BL21 cells (**Figure 4e and Figures S40-S43**). These results show that the cerium-dependent photoenzyme is compatible with whole-cell biocatalysis and may be further developed towards lignin degradation.

Cerium photoredox catalysis with a natural lanthanide-dependent enzyme

Over the last years, several lanthanide-dependent enzymes have been found in nature and were characterized in detail, with high-resolution structures being available.[25] We wondered whether these natural proteins may also be applied for cerium photoredox catalysis and chose the lanthanide-dependent alcohol dehydrogenase PedH from *Pseudomonas putida* KT2440 as a test case. The enzyme utilizes the redox cofactor pyrroloquinoline quinone (PQQ), which is only active when interacting with a Lewis acidic lanthanide ion in the active site. We expressed a previously engineered variant of PedH[41] recombinantly in *E. coli* and reconstituted the apo-enzyme with $CeCl_3$, but added no PQQ. The rationale was that the free space in the PQQ binding pocket may then be occupied by our diol substrates, which was supported by substrate docking results (**Figure 5a** and **Video S2**)

The binding affinity of PedH for Ce(III) was measured in displacement titrations against Tb(III) using tryptophan-enhanced terbium luminescence as a readout. Even in the absence of PQQ, PedH was found to bind the lanthanide ions with nanomolar affinity (**Figures S44/S45**).

Next, we performed the photocatalytic diol cleavage of **(*R,R*)-1** using cerium-bound PedH in comparison to **PLZ1.4** as a positive control and bovine serum albumin (BSA) as a negative control. PedH gave similar yields as **PLZ1.4** after 6 hours of irradiation, but turned out to be less photostable (**Figure 5b**). These results show that also natural lanthanide binding proteins may be utilized for enzymatic cerium photoredox catalysis. However, the de novo scaffold's robustness brings a clear advantage.

Discussion

Our results demonstrate that cerium photoredox catalysis can be performed efficiently inside of suitable protein scaffolds that possess a lanthanide binding site. The newly generated photoenzymes catalyze radical C-C bond cleavages. After this proof of concept, we optimized the catalysts, investigated mechanistic details, and explored potential applications.

Forming radical species in the presence of oxygen, we initially observed severe photodamage of the de novo scaffold, but could increase its photostability by protein engineering. Here, it was crucial to remove the tryptophan residues in close proximity to the metal binding site. We also demonstrated that the protein environment is able to induce initial stereocontrol in these radical reactions, notably with opposite enantiopreference for two of the PLZ variants. Even though the selectivities are not yet practically useful for kinetic resolutions, we generated a starting point for further enzyme engineering. We also made first steps towards another potential application of *PhotoLanZymes*, namely the degradation of lignin into synthetically valuable building blocks. This important challenge towards sustainable chemistry has been targeted previously by separate photocatalytic[38,42,43] or enzymatic[37,44] approaches, but not yet with a hybrid photobiocatalyst.

Photoenzymatic catalysis has gained momentum in recent years.[3] Natural redox enzymes have been shown to catalyze new-to-nature radical chemistry in the presence of light,[45-49] but also rationally designed photoenzymes have been generated successfully, for instance by covalently attaching a photocatalytic moiety[50-52] or even by genetically encoding a triplet sensitizer.[7,8,53,54] However, in most cases, the reactions have to be performed under inert reaction conditions. Our work adds a new mode of action to the photoenzymatic toolbox, namely cerium photoredox catalysis, which is compatible with whole-cell biocatalysis and aerobic conditions. The scope of this chemistry goes far beyond the diol cleavages shown here. Based on our results, cerium-dependent photoenzymes for stereoselective C-H activation and C-C bond forming reactions, which proceed via alkyl or aryl radicals, may be developed next. To that end, the choice of protein scaffold will be crucial. Our de novo TIM barrel binds lanthanides with very high affinity, but the large cavity size and high flexibility of the domain-connecting linkers turned out be a limitation when aiming for precise stereocontrol in the substrate binding site. Our ongoing efforts thus focus on evaluating alternative scaffolds, considering both natural as well as de novo proteins. For the

latter, we see great potential in applying the recently developed AI-based protein design tools (AlphaFold2, RoseTTAFold, RF diffusion and ProteinMPNN), which bring the field closer to the ultimate goal of building robust and tailor-made de novo proteins around just any active site of choice.[55-58]

Even with the perfect protein scaffold in hand, fine-tuning the photoenzymes' catalytic parameters will still need experimental optimization.[4,5,59] One of the most efficient ways to do so is directed evolution by in vivo selection. Here, we implemented an *E. coli* surface display strategy, which allows us to form artificial cerium enzymes in the context of whole cells. Having this tool available, the next step towards in vivo selection is to couple the survival of the cells to a cerium and light-dependent enzymatic activity. We believe that this approach will facilitate the development of artificial cerium enzymes for a broad range of synthetically valuable photoredox transformations.

Methods

Molecular cloning, recombinant expression and protein purification

Synthetic genes coding for PLZ variants, which are derived from our previously reported de novo protein scaffold TFD-EE,[22] and the natural alcohol dehydrogenase PedH[41] were purchased from Twist Bioscience. The sequences coding for OmpA and the Lpp signal peptide were amplified from genomic *E. coli* DNA. All constructs were assembled and subcloned into pET17 or pET29b expression vectors using a Gibson assembly protocol. Sequences of all constructs as well as primers used to introduce single point mutations are available in the **SI**.

The proteins were produced recombinantly in *E. coli* BL21-Gold(DE3) or *E. coli* SoluBL21 and then purified by affinity chromatography followed by size-exclusion chromatography (SEC). Residual metal ions bound to the proteins were removed by incubation in EDTA-containing buffer or dialysis in the presence of Chelex 100 resin. Strep-tagged PLZ variants were purified over a Strep-Tactin column and a Superdex 75 column. His-tagged PedH was purified over a Ni-NTA column and a Superdex 200 column. Purity and integrity of all proteins were evaluated by SDS-PAGE, protein mass spectrometry, and CD spectroscopy. Detailed protocols are available in the **SI**.

Photoenzymatic reactions

The protein (c = 111 µM) was incubated with one equivalent of $CeCl_3$ for 2.5 h at 40 °C in reaction buffer (25 mM HEPES, 100 mM NaCl, pH 8.5) to facilitate efficient metal binding. 90 µL of this solution were transferred to a glass vial and 10 µL substrate (c = 20 mM in acetonitrile) were added to reach final concentrations of 100 µM metalloenzyme, 2 mM substrate, and 10% (v/v) acetonitrile. Photoenzymatic reactions were carried out in customized, temperature-controlled photoreactors equipped with six LEDs (410–420 nm, 3 W), each one irradiating an individual glass vial in a reproducible fashion (**Figure S1**). After the overnight reaction, protein was precipitated by adding 100 µL acetonitrile and removed by centrifugation. Product yields were determined by HPLC, either by direct UV absorption for aromatic substrates or after derivatization with 2-amino-benzamidoxime (ABAO)[32] for aliphatic substrates. Calibration curves were generated using authentic standards (see **SI** for details).

Michaelis-Menten kinetics were determined by irradiating reaction mixtures containing 50 µM metalloenzyme and 0–12 mM substrate for 4 h. The stereoselectivity of the

photoenzyme was evaluated by separating unreacted substrate stereoisomers on a chiral column and quantifying their ratios for the enzyme-catalyzed reaction and the buffer control. Measurements were performed in triplicates.

Lanthanide binding measurements

Lanthanide binding was measured by tryptophan-enhanced terbium(III) luminescence.[22,26] The respective PLZ variants as well as PedH contain tryptophan residues in close proximity to the metal binding site, thereby enabling energy transfer to the lanthanide ion after excitation at 280 nm (**Figure S9**). The characteristic terbium(III) luminescence was recorded at 545 nm using a Varioskan LUX plate reader (Thermo Fisher Scientific) in time-resolved fluorescence (TRF) mode. This readout was also used to quantify cerium(III) binding in displacement titrations against terbium(III). Detailed protocols including the protein and lanthanide concentrations, pre-incubation times, and data fitting procedures for the different titrations or time-course measurements are available in the **SI**.

Photostability studies

The effects of photodamage in the enzyme variants were characterized by SDS-PAGE, analytical SEC, and protein mass spectrometry after long-term irradiation in the photoreactor. To that end, 200 µL metalloenzyme solution were prepared as described above. After incubating the protein with $CeCl_3$, 100 µL were kept in the dark at 4 °C, whereas the other 100 µL were irradiated for 24 h in the absence of substrate. For SDS-PAGE analysis, the samples were denatured and separated on a 4–20% Mini-PROTEAN TGX precast protein gel. Analytical SEC was performed in reaction buffer using a Superdex 75 Increase 10/300 GL column and a 100 µL injection loop. Protein mass spectrometry was performed by electrospray ionization on a SYNAPT XS High Resolution Mass Spectrometer (Waters). 2 µL protein sample (c = 0.1 mg/mL) were injected and separated on an ACQUITY UPLC Protein BEH C4 column using a linear gradient of 5% (v/v) to 85% (v/v) acetonitrile in water with a flow rate of 0.4 mL/min at 65 °C. The MassLynx v4.2 software was used for data analysis.

Mechanistic experiments

To trap proposed radical intermediates, photoenzymatic reactions were performed in the presence of 10 mM TEMPO as a radical scavenger. Adducts were identified by

LC-MS, using an Agilent 1290 Infinity II uHPLC instrument equipped with a diode array detector, a single-quadrupole detector, and a Jet Stream ionization source (Agilent Technologies).

Isotope labeling experiments were performed by running the photoenzymatic reaction in $H_2{}^{18}O$. To that end, metalloenzyme and buffer were lyophilized beforehand. Samples were extracted and the incorporation of ^{18}O into benzaldehyde and benzyl alcohol was analyzed by GC-MS (Agilent GC-7890B with MSD-5977A, Agilent Technologies)

Cell surface display and whole-cell photobiocatalysis

A fusion construct coding for PLZ1.1 with an N-terminal Lpp-OmpA sequence for outer membrane integration and a C-terminal HA-tag for immunofluorescence detection was cloned and expressed in *E. coli* BL21-Gold(DE3). The display efficiency was evaluated by fluorescence microscopy and Western blot analysis. Detailed protocols are available in the **SI**.

For whole-cell photobiocatalysis, cells expressing the fusion construct were harvested by centrifugation, resuspended in buffer containing 500 µM $CeCl_3$, and incubated for 2 h at 37 °C and 700 rpm. To remove unspecifically bound Ce(III), cells were washed twice and then resuspended in reaction buffer (25 mM HEPES, pH 8.5, 100 mM NaCl). Photoreactions with 2 mM lignin surrogate **24** as the substrate were performed in the photoreactor as described above. However, instead of purified enzyme, the samples now contained whole *E. coli* cells at OD_{600} = 25 as the catalyst.

References

1 Buller, R., Lutz, S., Kazlauskas, R. J., Snajdrova, R., Moore, J. C. & Bornscheuer, U. T. From nature to industry: Harnessing enzymes for biocatalysis. *Science* **382**, eadh8615 (2023).

2 Schwizer, F., Okamoto, Y., Heinisch, T., Gu, Y., Pellizzoni, M. M., Lebrun, V., Reuter, R., Kohler, V., Lewis, J. C. & Ward, T. R. Artificial metalloenzymes: Reaction scope and optimization strategies. *Chem. Rev.* **118**, 142-231 (2018).

3 Emmanuel, M. A., Bender, S. G., Bilodeau, C., Carceller, J. M., DeHovitz, J. S., Fu, H., Liu, Y., Nicholls, B. T., Ouyang, Y., Page, C. G., Qiao, T., Raps, F. C., Sorigue, D. R., Sun, S. Z., Turek-Herman, J., Ye, Y., Rivas-Souchet, A., Cao, J. & Hyster, T. K. Photobiocatalytic strategies for organic synthesis. *Chem. Rev.* **123**, 5459-5520 (2023).

4 Zeymer, C. & Hilvert, D. Directed evolution of protein catalysts. *Annu. Rev. Biochem.* **87**, 131-157 (2018).

5 Wang, Y., Xue, P., Cao, M., Yu, T., Lane, S. T. & Zhao, H. Directed evolution: Methodologies and applications. *Chem. Rev.* **121**, 12384-12444 (2021).

6 Basler, S., Studer, S., Zou, Y., Mori, T., Ota, Y., Camus, A., Bunzel, H. A., Helgeson, R. C., Houk, K. N., Jiménez-Osés, G. & Hilvert, D. Efficient lewis acid catalysis of an abiological reaction in a de novo protein scaffold. *Nat. Chem.* **13**, 231-235 (2021).

7 Trimble, J. S., Crawshaw, R., Hardy, F. J., Levy, C. W., Brown, M. J. B., Fuerst, D. E., Heyes, D. J., Obexer, R. & Green, A. P. A designed photoenzyme for enantioselective [2+2] cycloadditions. *Nature* **611**, 709-714 (2022).

8 Sun, N., Huang, J., Qian, J., Zhou, T. P., Guo, J., Tang, L., Zhang, W., Deng, Y., Zhao, W., Wu, G., Liao, R. Z., Chen, X., Zhong, F. & Wu, Y. Enantioselective [2+2]-cycloadditions with triplet photoenzymes. *Nature* **611**, 715-720 (2022).

9 Prier, C. K., Rankic, D. A. & MacMillan, D. W. Visible light photoredox catalysis with transition metal complexes: Applications in organic synthesis. *Chem. Rev.* **113**, 5322-5363 (2013).

10 Cheisson, T. & Schelter, E. J. Rare earth elements: Mendeleev's bane, modern marvels. *Science* **363**, 489-493 (2019).

11 Qiao, Y. & Schelter, E. J. Lanthanide photocatalysis. *Acc. Chem. Res.* **51**, 2926-2936 (2018).

12 Abundance of elements in the earth's crust and in the sea, CRC handbook of chemistry and physics, 97th edition (2016–2017), p. 14-17.

13 Yin, H., Jin, Y., Hertzog, J. E., Mullane, K. C., Carroll, P. J., Manor, B. C., Anna, J. M. & Schelter, E. J. The hexachlorocerate(III) anion: A potent, benchtop stable, and readily available ultraviolet A photosensitizer for aryl chlorides. *J. Am. Chem. Soc.* **138**, 16266-16273 (2016).

14 Qiao, Y., Yang, Q. & Schelter, E. J. Photoinduced Miyaura borylation by a rare-earth-metal photoreductant: The hexachlorocerate(III) anion. *Angew. Chem. Int. Ed.* **57**, 10999-11003 (2018).

15 Hu, A., Guo, J. J., Pan, H. & Zuo, Z. Selective functionalization of methane, ethane, and higher alkanes by cerium photocatalysis. *Science* **361**, 668-672 (2018).

16 An, Q., Wang, Z., Chen, Y., Wang, X., Zhang, K., Pan, H., Liu, W. & Zuo, Z. Cerium-catalyzed C-H functionalizations of alkanes utilizing alcohols as hydrogen atom transfer agents. *J. Am. Chem. Soc.* **142**, 6216-6226 (2020).

17 Yang, Q., Wang, Y. H., Qiao, Y., Gau, M., Carroll, P. J., Walsh, P. J. & Schelter, E. J. Photocatalytic C-H activation and the subtle role of chlorine radical complexation in reactivity. *Science* **372**, 847-852 (2021).

18 An, Q., Xing, Y.-Y., Pu, R., Jia, M., Chen, Y., Hu, A., Zhang, S.-Q., Yu, N., Du, J., Zhang, Y., Chen, J., Liu, W., Hong, X. & Zuo, Z. Identification of alkoxy radicals as hydrogen atom transfer agents in Ce-catalyzed C-H functionalization. *J. Am. Chem. Soc.* **145**, 359-376 (2023).

19 Klein, A. S. & Zeymer, C. Design and engineering of artificial metalloproteins: From de novo metal coordination to catalysis. *Protein Eng. Des. Sel.* **34**, gzab003 (2021).

20 Chalkley, M. J., Mann, S. I. & DeGrado, W. F. De novo metalloprotein design. *Nat. Rev. Chem.* **6**, 31-50 (2022).

21 Huang, P. S., Feldmeier, K., Parmeggiani, F., Velasco, D. A. F., Höcker, B. & Baker, D. De novo design of a four-fold symmetric TIM-barrel protein with atomic-level accuracy. *Nat. Chem. Biol.* **12**, 29-34 (2016).
22 Caldwell, S. J., Haydon, I. C., Piperidou, N., Huang, P. S., Bick, M. J., Sjöström, H. S., Hilvert, D., Baker, D. & Zeymer, C. Tight and specific lanthanide binding in a de novo TIM barrel with a large internal cavity designed by symmetric domain fusion. *Proc. Natl. Acad. Sci. U.S.A.* **117**, 30362-30369 (2020).
23 Cotruvo, J. A., Jr., Featherston, E. R., Mattocks, J. A., Ho, J. V. & Laremore, T. N. Lanmodulin: A highly selective lanthanide-binding protein from a lanthanide-utilizing bacterium. *J. Am. Chem. Soc.* **140**, 15056-15061 (2018).
24 Jahn, B., Pol, A., Lumpe, H., Barends, T. R. M., Dietl, A., Hogendoorn, C., Op den Camp, H. J. M. & Daumann, L. J. Similar but not the same: First kinetic and structural analyses of a methanol dehydrogenase containing a europium ion in the active site. *ChemBioChem* (2018).
25 Daumann, L. J. Essential and ubiquitous: The emergence of lanthanide metallobiochemistry. *Angew. Chem. Int. Ed.* **58**, 12795-12802 (2019).
26 Mattocks, J. A., Tirsch, J. L. & Cotruvo, J. A., Jr. Determination of affinities of lanthanide-binding proteins using chelator-buffered titrations. *Methods Enzymol.* **651**, 23-61 (2021).
27 Schwarz, J. & König, B. Visible-light mediated C-C bond cleavage of 1,2-diols to carbonyls by cerium-photocatalysis. *Chem. Commun.* **55**, 486-488 (2019).
28 Asquith, R. S. & Rivett, D. E. Studies on the photooxidation of tryptophan. *Biochim. Biophys. Acta* **252**, 111-116 (1971).
29 Reid, L. O., Roman, E. A., Thomas, A. H. & Dántola, M. L. Photooxidation of tryptophan and tyrosine residues in human serum albumin sensitized by pterin: A model for globular protein photodamage in skin. *Biochemistry* **55**, 4777-4786 (2016).
30 Bellmaine, S., Schnellbaecher, A. & Zimmer, A. Reactivity and degradation products of tryptophan in solution and proteins. *Free Radical Biol. Med.* **160**, 696-718 (2020).
31 Sánchez-Aparicio, J.-E., Tiessler-Sala, L., Velasco-Carneros, L., Roldán-Martín, L., Sciortino, G. & Maréchal, J.-D. *BioMetAll*: Identifying metal-binding sites in proteins from backbone preorganization. *J. Chem. Inf. Model.* **61**, 311-323 (2021).
32 Ressmann, A. K., Schwendenwein, D., Leonhartsberger, S., Mihovilovic, M. D., Bornscheuer, U. T., Winkler, M. & Rudroff, F. Substrate-independent high-throughput assay for the quantification of aldehydes. *Adv. Synth. Catal.* **361**, 2538-2543 (2019).
33 Jumper, J., Evans, R., Pritzel, A., Green, T., Figurnov, M., Ronneberger, O., Tunyasuvunakool, K., Bates, R., Žídek, A., Potapenko, A., Bridgland, A., Meyer, C., Kohl, S. A. A., Ballard, A. J., Cowie, A., Romera-Paredes, B., Nikolov, S., Jain, R., Adler, J., Back, T., Petersen, S., Reiman, D., Clancy, E., Zielinski, M., Steinegger, M., Pacholska, M., Berghammer, T., Bodenstein, S., Silver, D., Vinyals, O., Senior, A. W., Kavukcuoglu, K., Kohli, P. & Hassabis, D. Highly accurate protein structure prediction with AlphaFold. *Nature* **596**, 583-589 (2021).
34 Mirdita, M., Schütze, K., Moriwaki, Y., Heo, L., Ovchinnikov, S. & Steinegger, M. Colabfold: Making protein folding accessible to all. *Nat. Methods* **19**, 679-682 (2022).
35 Subbotina, E., Rukkijakan, T., Marquez-Medina, M. D., Yu, X., Johnsson, M. & Samec, J. S. M. Oxidative cleavage of C-C bonds in lignin. *Nat. Chem.* **13**, 1118-1125 (2021).
36 Erickson, E., Bleem, A., Kuatsjah, E., Werner, A. Z., DuBois, J. L., McGeehan, J. E., Eltis, L. D. & Beckham, G. T. Critical enzyme reactions in aromatic catabolism for microbial lignin conversion. *Nat. Catal.* **5**, 86-98 (2022).
37 Chan, J. C., Paice, M. & Zhang, X. Enzymatic oxidation of lignin: Challenges and barriers toward practical applications. *ChemCatChem* **12**, 401-425 (2020).
38 Liu, H., Li, H., Luo, N. & Wang, F. Visible-light-induced oxidative lignin C-C bond cleavage to aldehydes using vanadium catalysts. *ACS Catal.* **10**, 632-643 (2020).
39 Wang, Y., He, J. & Zhang, Y. $CeCl_3$-promoted simultaneous photocatalytic cleavage and amination of C(alpha)-C(beta) bond in lignin model compounds and native lignin. *CCS Chem.* **2**, 107-117 (2020).

40 Heinisch, T., Schwizer, F., Garabedian, B., Csibra, E., Jeschek, M., Vallapurackal, J., Pinheiro, V. B., Marlière, P., Panke, S. & Ward, T. R. E. Coli surface display of streptavidin for directed evolution of an allylic deallylase. *Chem. Sci.* **9**, 5383-5388 (2018).
41 Wehrmann, M., Elsayed, E. M., Kobbing, S., Bendz, L., Lepak, A., Schwabe, J., Wierckx, N., Bange, G. & Klebensberger, J. Engineered PQQ-dependent alcohol dehydrogenase for the oxidation of 5-(hydroxymethyl)furoic acid. *ACS Catal.* **10**, 7836-7842 (2020).
42 Nguyen, J. D., Matsuura, B. S. & Stephenson, C. R. J. A photochemical strategy for lignin degradation at room temperature. *J. Am. Chem. Soc.* **136**, 1218-1221 (2014).
43 Xu, E., Xie, F., Liu, T., He, J. & Zhang, Y. Photocatalytic, oxidative cleavage of C-C bond in lignin models and native lignin. *Chem. Eur. J.*, e202304209 (2024).
44 Bugg, T. D. H., Williamson, J. J. & Rashid, G. M. M. Bacterial enzymes for lignin depolymerisation: New biocatalysts for generation of renewable chemicals from biomass. *Curr. Opin. Chem. Biol.* **55**, 26-33 (2020).
45 Emmanuel, M. A., Greenberg, N. R., Oblinsky, D. G. & Hyster, T. K. Accessing non-natural reactivity by irradiating nicotinamide-dependent enzymes with light. *Nature* **540**, 414-417 (2016).
46 Biegasiewicz, K. F., Cooper, S. J., Gao, X., Oblinsky, D. G., Kim, J. H., Garfinkle, S. E., Joyce, L. A., Sandoval, B. A., Scholes, G. D. & Hyster, T. K. Photoexcitation of flavoenzymes enables a stereoselective radical cyclization. *Science* **364**, 1166-1169 (2019).
47 Huang, X., Wang, B., Wang, Y., Jiang, G., Feng, J. & Zhao, H. Photoenzymatic enantioselective intermolecular radical hydroalkylation. *Nature* **584**, 69-74 (2020).
48 Nicholls, B. T., Oblinsky, D. G., Kurtoic, S. I., Grosheva, D., Ye, Y., Scholes, G. D. & Hyster, T. K. Engineering a non-natural photoenzyme for improved photon efficiency. *Angew Chem Int Ed Engl* **61**, e202113842 (2022).
49 Ye, Y., Cao, J., Oblinsky, D. G., Verma, D., Prier, C. K., Scholes, G. D. & Hyster, T. K. Using enzymes to tame nitrogen-centred radicals for enantioselective hydroamination. *Nat. Chem.* **15**, 206-212 (2023).
50 Gu, Y., Ellis-Guardiola, K., Srivastava, P. & Lewis, J. C. Preparation, characterization, and oxygenase activity of a photocatalytic artificial enzyme. *ChemBioChem* **16**, 1880-1883 (2015).
51 Zubi, Y. S., Liu, B., Gu, Y., Sahoo, D. & Lewis, J. C. Controlling the optical and catalytic properties of artificial metalloenzyme photocatalysts using chemogenetic engineering. *Chem. Sci.* **13**, 1459-1468 (2022).
52 Kuckhoff, T., Brewster, R. C., Ferguson, C. T. J. & Jarvis, A. G. Reactivity tuning of metal-free artificial photoenzymes through binding site specific bioconjugation. *Eur. J. Org. Chem.* **26**, e202201412 (2023).
53 Liu, X., Kang, F., Hu, C., Wang, L., Xu, Z., Zheng, D., Gong, W., Lu, Y., Ma, Y. & Wang, J. A genetically encoded photosensitizer protein facilitates the rational design of a miniature photocatalytic CO_2-reducing enzyme. *Nat. Chem.* **10**, 1201-1206 (2018).
54 Fu, Y., Huang, J., Wu, Y., Liu, X., Zhong, F. & Wang, J. Biocatalytic cross-coupling of aryl halides with a genetically engineered photosensitizer artificial dehalogenase. *J. Am. Chem. Soc.* **143**, 617-622 (2021).
55 Baek, M., DiMaio, F., Anishchenko, I., Dauparas, J., Ovchinnikov, S., Lee, G. R., Wang, J., Cong, Q., Kinch, L. N., Schaeffer, R. D., Millán, C., Park, H., Adams, C., Glassman, C. R., DeGiovanni, A., Pereira, J. H., Rodrigues, A. V., van Dijk, A. A., Ebrecht, A. C., Opperman, D. J., Sagmeister, T., Buhlheller, C., Pavkov-Keller, T., Rathinaswamy, M. K., Dalwadi, U., Yip, C. K., Burke, J. E., Garcia, K. C., Grishin, N. V., Adams, P. D., Read, R. J. & Baker, D. Accurate prediction of protein structures and interactions using a three-track neural network. *Science* **373**, 871-876 (2021).
56 Watson, J. L., Juergens, D., Bennett, N. R., Trippe, B. L., Yim, J., Eisenach, H. E., Ahern, W., Borst, A. J., Ragotte, R. J., Milles, L. F., Wicky, B. I. M., Hanikel, N., Pellock, S. J., Courbet, A., Sheffler, W., Wang, J., Venkatesh, P., Sappington, I., Torres, S. V., Lauko, A., De Bortoli, V., Mathieu, E., Ovchinnikov, S., Barzilay, R., Jaakkola, T. S., DiMaio, F., Baek, M. & Baker, D. De novo design of protein structure and function with RFdiffusion. *Nature* **620**, 1089-1100 (2023).

57 Dauparas, J., Anishchenko, I., Bennett, N., Bai, H., Ragotte, R. J., Milles, L. F., Wicky, B. I. M., Courbet, A., de Haas, R. J., Bethel, N., Leung, P. J. Y., Huddy, T. F., Pellock, S., Tischer, D., Chan, F., Koepnick, B., Nguyen, H., Kang, A., Sankaran, B., Bera, A. K., King, N. P. & Baker, D. Robust deep learning–based protein sequence design using ProteinMPNN. *Science* **378**, 49-56 (2022).

58 Krishna, R., Wang, J., Ahern, W., Sturmfels, P., Venkatesh, P., Kalvet, I., Lee, G. R., Morey-Burrows, F. S., Anishchenko, I., Humphreys, I. R., McHugh, R., Vafeados, D., Li, X., Sutherland, G. A., Hitchcock, A., Hunter, C. N., Baek, M., DiMaio, F. & Baker, D. Generalized biomolecular modeling and design with RoseTTAFold all-atom. *bioRxiv* (2023).

59 Wittwer, M., Markel, U., Schiffels, J., Okuda, J., Sauer, D. F. & Schwaneberg, U. Engineering and emerging applications of artificial metalloenzymes with whole cells. *Nat. Catal.* **4**, 814-827 (2021).

Acknowledgements

This work was funded by an ERC Starting Grant (*PhotoLanZyme*, project number: 101039592). F.L.M. received a PhD fellowship of the German Academic Scholarship Foundation. B.B. received the Kekulé fellowship of the FCI. The project was also supported by the German Research Foundation (DFG, project number: 453748800). We thank the Swiss National Science Foundation (SNSF) for funding the initial project phase with a Spark Grant (project number: 190383). We are grateful to Carolin Rulofs, Ruth Hillermann, Laura Meier, Anna Pastucha, and Jürgen Kudermann for technical support with protein purification, protein mass spectrometry, fluorescence microscopy, and GC-MS measurements, respectively. We acknowledge the Leibniz Supercomputing Center for providing computational resources and access to the Schrödinger software and thank Burkhard König and Golo Storch for critical feedback on the manuscript.

Author contributions

C.Z. conceived and directed the project. A.S.K. and F.L.M. designed, performed, and analyzed the majority of all experiments, including chemical synthesis, molecular cloning, protein purification, photoenzymatic reactions, photostability studies, and mechanistic experiments with all PLZ variants. R.M. established the cell surface display of the photoenzyme and performed whole-cell biocatalysis. B.B. and H.K. performed the experiments with the natural lanthanide-binding protein PedH. G.M. carried out computational work, including protein surface engineering and substrate docking. C.Z. and A.S.K. wrote the manuscript and the SI, with input from all other authors.

Competing interests

The authors declare no competing interests.

Figures / Tables

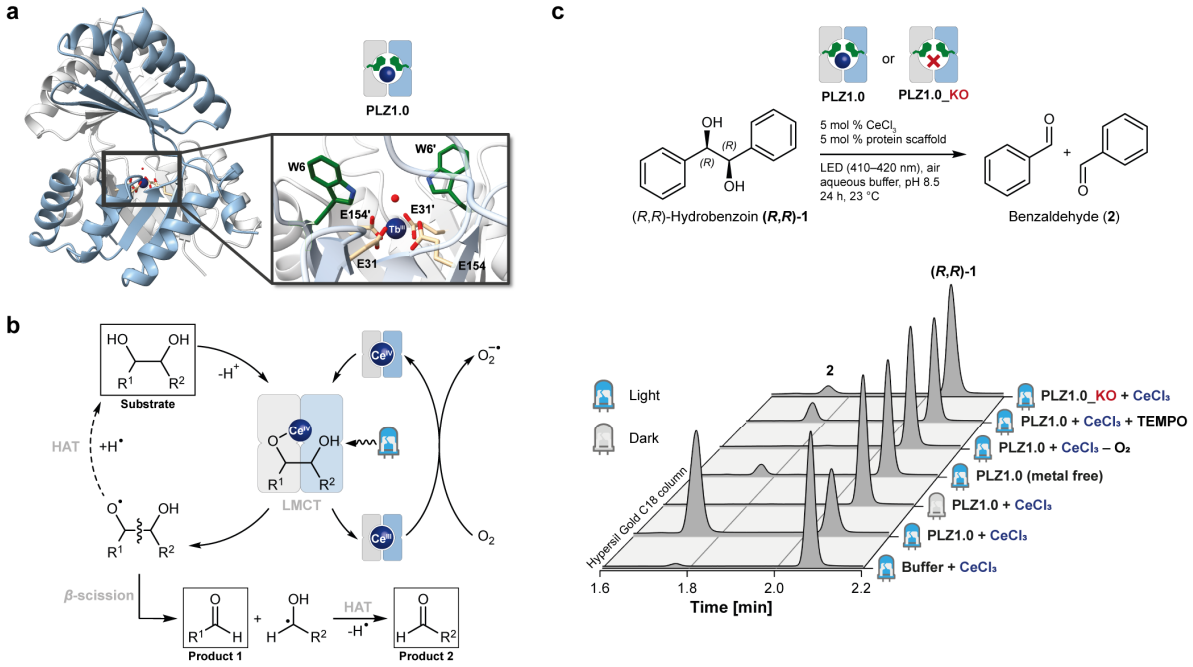

Figure 1. Cerium photoredox catalysis in a lanthanide-binding de novo protein. **(a)** Crystal structure of the TFD scaffold (= PLZ1.0 or *PhotoLanZyme* 1.0), here shown in complex with Tb(III). The dimeric TIM barrel scaffold possesses a lanthanide binding site that consists of 2 x 2 coordinating glutamate residues. Close-by tryptophan residues were installed to measure lanthanide binding via sensitized Tb(III) luminescence. PDB entry: 6ZV9.[22] **(b)** Proposed mechanism for a radical 1,2-diol cleavage catalyzed by a Ce(III/IV)-dependent artificial photoenzyme. LMCT = ligand-to-metal charge transfer, HAT = hydrogen atom transfer. **(c)** Proof of concept: Cerium-bound PLZ1.0 catalyzes the photocatalytic cleavage of hydrobenzoin (**1**) to benzaldehyde (**2**). The reaction was monitored by HPLC. Controls include samples without protein, without irradiation, without $CeCl_3$, without oxygen, with TEMPO as a radical scavenger, and using a metal binding deficient knock-out variant (PLZ1.0_KO).

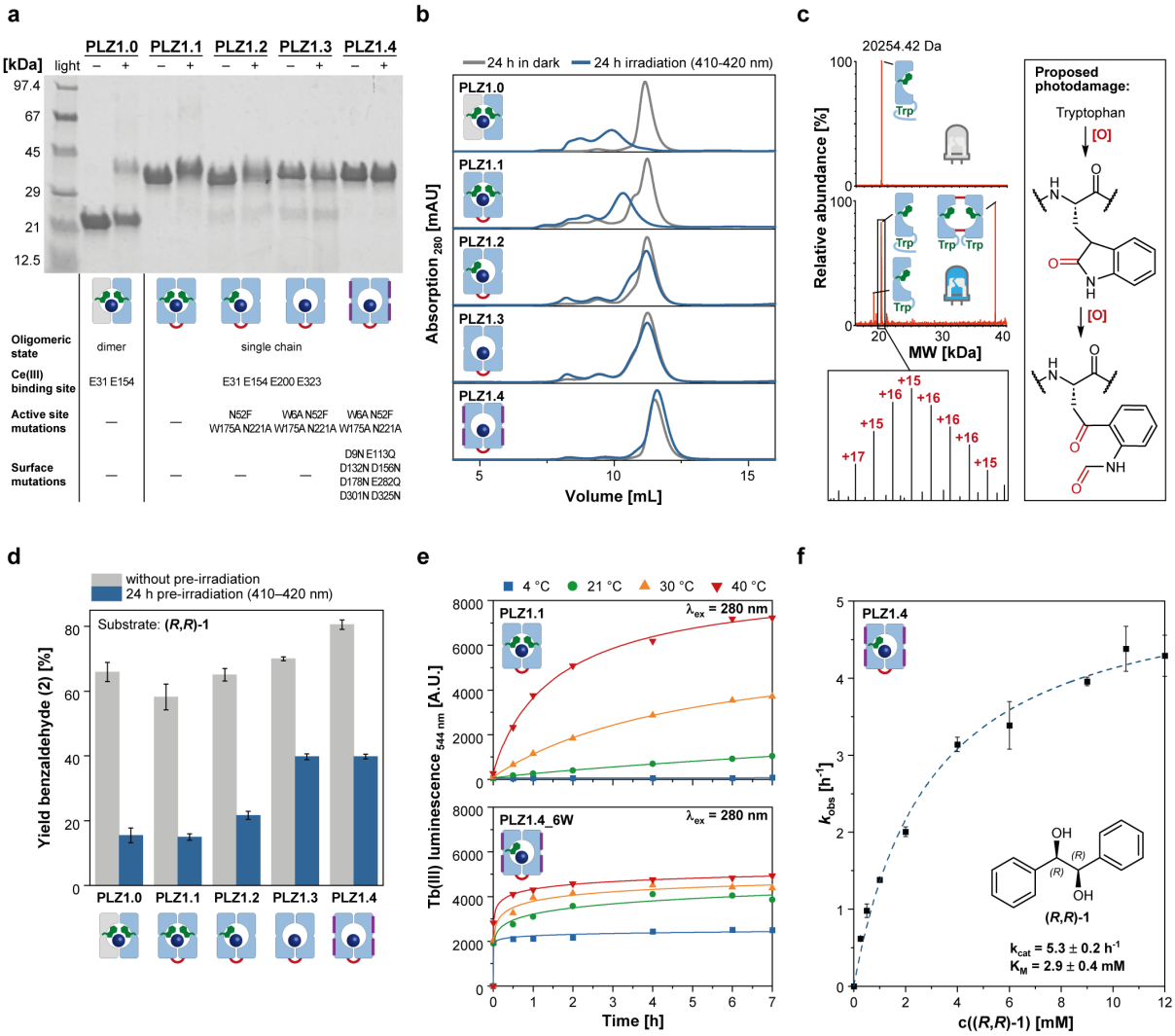

Figure 2. Optimization of photostability and metal binding behavior by protein engineering. **(a/b)** Photodamage of enzyme variants PLZ1.1 to PLZ1.4 after overnight irradiation in the presence of $CeCl_3$ monitored by SDS-PAGE (A) and analytical size exclusion chromatography (B). PLZ1.1 was generated by fusing the C-terminus of one monomer to the N-terminus of the other monomer. In PLZ1.2 and PLZ1.3, active-site tryptophans W6 and W175 were sequentially removed. PLZ1.4 contains further mutations on the protein surface. **(c)** Photodamage analysis by protein mass spectrometry of PLZ1.0 before and after irradiation in the presence of $CeCl_3$. **(d)** Photocatalytic performance of PLZ variants with and without pre-irradiation. **(e)** Influence of temperature and surface engineering on lanthanide binding kinetics measured by tryptophan-enhanced Tb(III) luminescence. Note: One of the previously removed active-site tryptophans (W6) had to be re-introduced into PLZ1.4 for these measurements. **(f)** Michaelis-Menten kinetics for the photoenzymatic cleavage of (*R,R*)-hydrobenzoin.

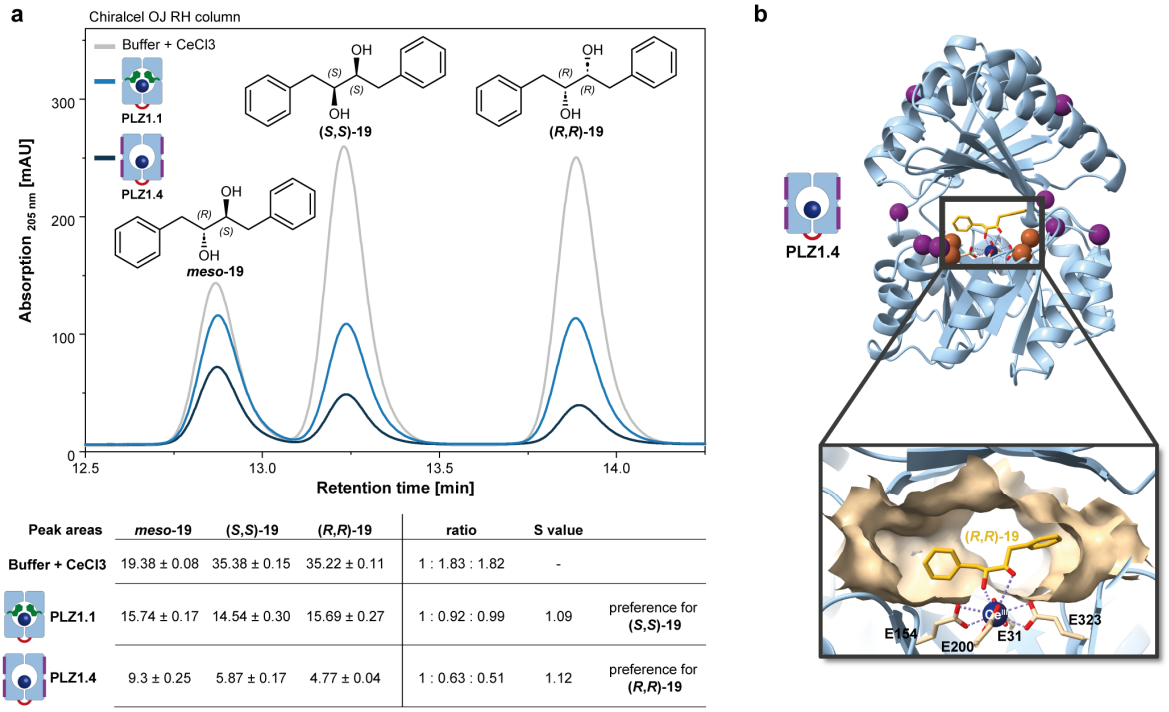

Peak areas	*meso*-19	(*S*,*S*)-19	(*R*,*R*)-19	ratio	S value	
Buffer + CeCl3	19.38 ± 0.08	35.38 ± 0.15	35.22 ± 0.11	1 : 1.83 : 1.82	-	
PLZ1.1	15.74 ± 0.17	14.54 ± 0.30	15.69 ± 0.27	1 : 0.92 : 0.99	1.09	preference for (*S*,*S*)-19
PLZ1.4	9.3 ± 0.25	5.87 ± 0.17	4.77 ± 0.04	1 : 0.63 : 0.51	1.12	preference for (*R*,*R*)-19

Figure 3. Initial stereoselectivity. **(a)** Chiral HPLC traces quantifying the three stereoisomers of unreacted diol substrate **19** after overnight photocatalysis. Measurements were performed in triplicates. In addition to a pronounced diastereoselectivity, PLZ1.1 and PLZ1.4 show an initial enantioselectivity with preference for the opposite enantiomer. The S value (calculated from *e.e*. and conversion) is low and not yet practically useful for kinetic resolutions. However, these results provide clear evidence that the photocatalytic reaction occurs inside the protein and that its stereochemical outcome is influenced by the binding pocket. **(b)** AlphaFold2 model of **PLZ1.4** in complex with Ce(III). Active-site mutations are shown in orange and surface modifications in purple. Docking of stereoisomers of substrate **19** (yellow) revealed that the cavity is much larger than the diol molecule and thus can bind it in various orientations.

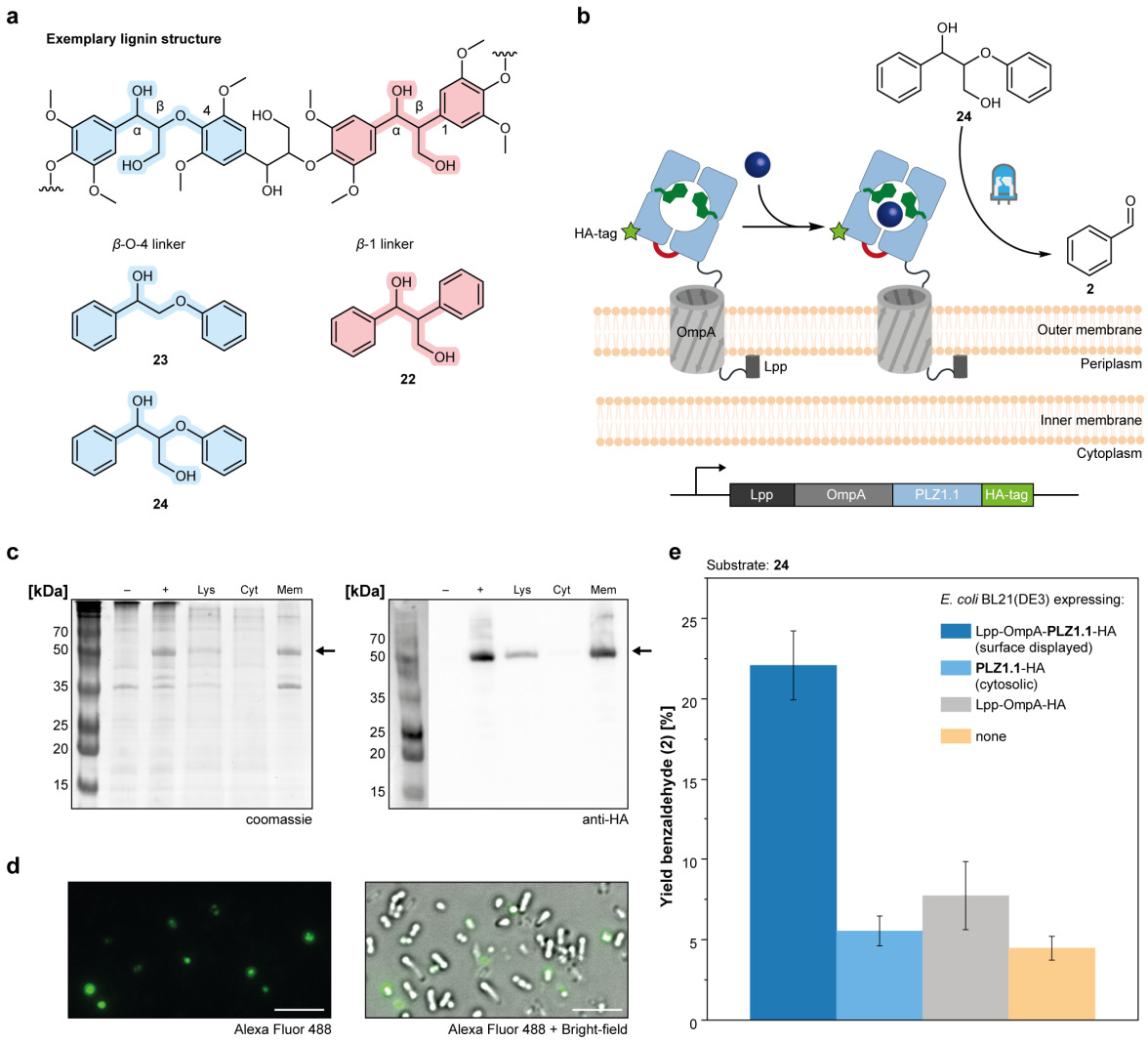

Figure 4. Whole-cell photobiocatalysis towards lignin degradation. **(a)** Exemplary structure of polymeric lignin and surrogates **22-24**, highlighting the most common linkages. **(b)** *E. coli* surface display of PLZ1.1 as a Lpp-OmpA fusion construct with a C-terminal HA tag. **(c)** SDS-PAGE and Western blot analysis of *E. coli* cells expressing Lpp-OmpA-PLZ1.1-HA. Samples before induction (-), after expression (+), cell lysate (Lys), cytoplasmic fraction (Cyt), and membrane fraction (Mem) are shown. The arrow indicates the molecular weight of the fusion construct. **(d)** Fluorescence microscopy of *E. coli* cells expressing Lpp-OmpA-PLZ1.1-HA. The cells were treated with a primary anti-HA antibody and a secondary fluorescent antibody. **(e)** Photocatalytic degradation of lignin surrogate **24** by whole cells incubated with $CeCl_3$. The yield of benzaldehyde (**2**) was determined in triplicates.

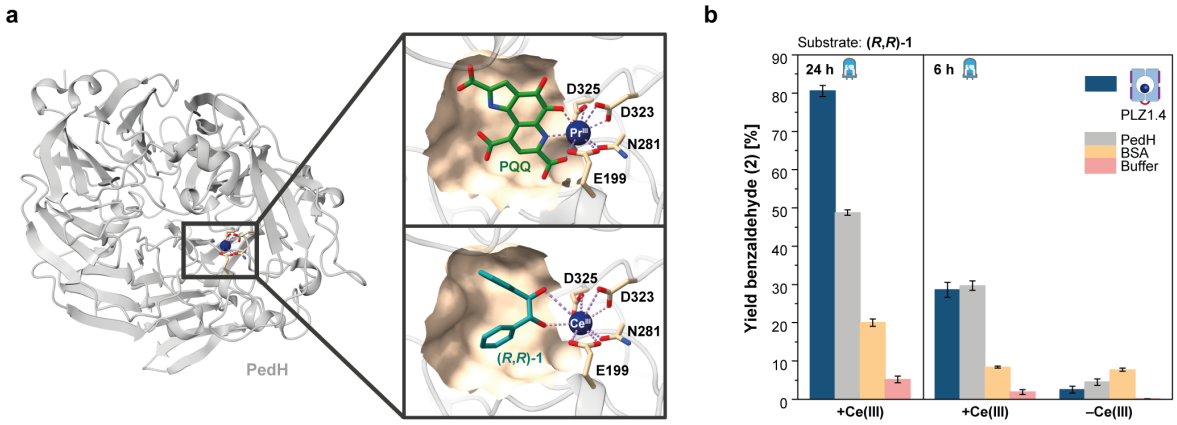

Figure 5. Photocatalytic diol cleavage by the natural lanthanide-dependent redox enzyme PedH from *P. putida*. **(a)** Crystal structure of a previously engineered variant of PedH (PDB entry: 6ZCV).[41] The alcohol dehydrogenase has a lanthanide binding site and utilizes the redox cofactor pyrroloquinoline quinone (PQQ). The natural active site is shown in the upper panel. The lower panel shows a docking model in which (*R,R*)-hydrobenzoin occupies the PQQ binding pocket. **(b)** Photocatalytic cleavage of hydrobenzoin (**1**) by PedH reconstituted with $CeCl_3$ in the absence of PQQ. The yields were compared to PLZ1.4 as the positive control and BSA as the negative control. Photostability was assessed by comparing the yields after 6 hours and 24 hours.

Table 1. Substrate scope. All photoenzymatic reactions were performed in aqueous buffer and under aerobic conditions upon irradiation at 410-420 nm for 24 hours with final concentrations of 100 µM metalloenzyme, 2 mM substrate, and 10% (v/v) acetonitrile. The yields were determined by HPLC. The accuracy (ca. +/- 3%) is limited by intensity variations between single LEDs in our photoreactors.

Substrate	**Product** (Yield [%] for PLZ1.4 / Buffer with $CeCl_3$)	**Substrate**	**Product** (Yield [%] for PLZ1.4 / Buffer with $CeCl_3$)
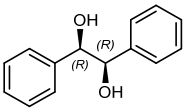 **(*R*,*R*)-1**	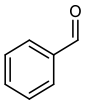 **2** (80 / 2)[a]	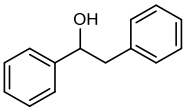 **12**	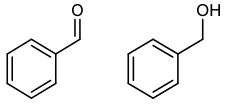 **2** (28 / trace) **13** (17 / 0)
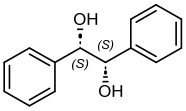 **(*S*,*S*)-1**		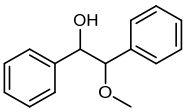 **14**	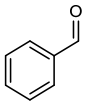 **2** (27 / trace)
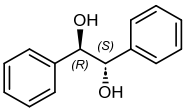 ***meso*-1**	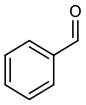 **2** (40 / trace)[a]	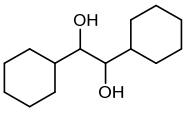 **15**	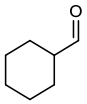 **16** (14 / trace)[a]
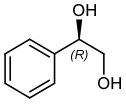 **(*R*)-3**	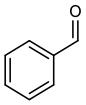 **2** (20 / trace)	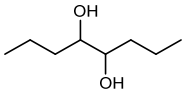 **17**	 **18** (5 / trace)[a]
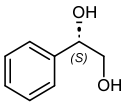 **(*S*)-3**		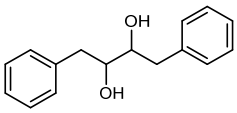 **19**	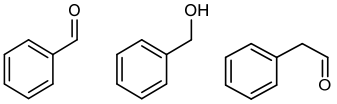 **2** (14 / trace)[a] **13** (12 / 0)[a] **20** (0 / 0)[a]
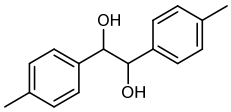 **4**	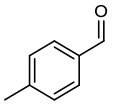 **5** (84 / 3)[a]	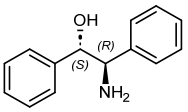 **21**	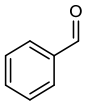 **2** (59 / trace)[a]
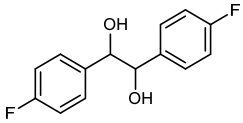 **6**	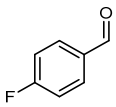 **7** (80 / 3)[a]	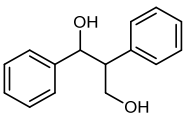 **22**	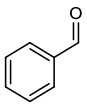 **2** (26 / trace)[a]
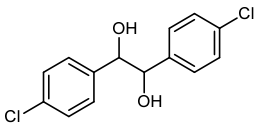 **8**	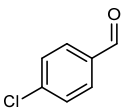 **9** (70 / 4)[a]	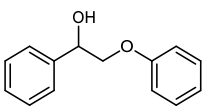 **23**	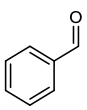 **2** (16 / 0)
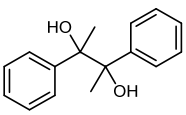 **10**	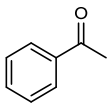 **11** (42 / trace)[a]	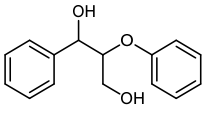 **24**	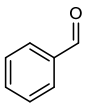 **2** (28 / trace)

[a] Yield corresponds to the expected formation two molecules of product per substrate.